Rapid solidification of silver-rich Ag-Cu-Zr alloys

Rapid solidification of silver-rich Ag–Cu–Zr alloys

A. Castellero[1,*], D.H. Kang[2,3], I.-H. Jung[2], G. Angella[4], M. Vedani[5], M. Baricco[1]

[1] Dipartimento di Chimica I.F.M. and N.I.S., Università di Torino, Torino, Italy

[2] Department of Mining and Materials Engineering, McGill University, Montreal, Quebec, Canada

[3] Novelis Global Technology Center, Kingston, Ontario, Canada

[4] Istituto per l'Energetica e le Interfasi, CNR-IENI, Milano, Italy

[5] Dipartimento di Meccanica, Politecnico di Milano, Milano, Italy

[*]corresponding author: Alberto Castellero, Tel: + 39 011 670 7097, Fax: + 39 011 670 7855

e-mail address: alberto.castellero@unito.it

Abstract

In this work we explored the possibility of obtaining amorphous/crystalline composites in the Ag-rich side of the Ag–Cu–Zr ternary system exploiting the presence of a miscibility gap in the liquid. Four alloys with nominal composition (at.%) $Ag_{75}Cu_{11}Zr_{14}$ (alloy A), $Ag_{73}Cu_{17}Zr_{10}$ (alloy B), $Ag_{47.5}Cu_{22.5}Zr_{30}$ (alloy C), $Ag_{47.5}Cu_{30}Zr_{22.5}$ (alloy D) were investigated. The effect of the cooling rate and the composition on phase selection and microstructures was evaluated by comparing slowly cooled master ingots and rapidly quenched ribbons. Evidence of the liquid miscibility gap was observed only in alloys B and D, either in the master ingots and the ribbons. After rapid solidification, partial amorphisation was achieved for alloys C and D, where precipitates of the Ag-rich solid solution, showing various sizes, are dispersed in the amorphous matrix. A significant increase in hardness was achieved in the case of partially amorphous ribbons of alloys C and D (442 HV and 533 HV, respectively). Experimental results are discussed on the basis of the recently reassessed ternary Ag-Cu-Zr phase diagram.

Keywords: amorphous alloys, rapid solidification, Ag-based alloys, calphad, microstructures

INTRODUCTION

It is well known that bulk metallic glasses (BMGs), or amorphous alloys, on the one hand are characterised by high yield strength and large elastic strain limit, and, on the other hand, they do not show plasticity in tension due to shear softening (i.e. plastic deformation occurring along bands with lowered viscosity) [1-2]. Improvement of the plastic deformation has been achieved, typically under a geometrical constraint (e.g. upon compression and bending), in BMG composites where second phase particles, such as ex-situ ceramic particles [3], in-situ coarse dendrites [4] or nanocrystalline precipitates [5-7], are homogeneously dispersed in the amorphous matrix.

The presence of a second phase (either amorphous or crystalline), forming a strong and intimate interface with the amorphous matrix, tends to promote the shear delocalisation by branching the individual shear bands and stops their propagation. The strain at failure of BMG composites strongly depends on the volume fraction, size, shape and distribution of the second phase inclusions. In the case of composites containing micron size ductile crystalline particles highly dispersed in the amorphous matrix, the shear band propagation is confined by the interparticle distance [4] and the ductile crystalline particles locally deform by dislocation mechanism [8], allowing plastic deformation either in compression and tension [9]. Second phase inclusions with a spherical shape can further improve the plastic deformation of the composites with respect to dendritic precipitates, as shown in ref. [10]. When the composite contains a fine dispersion of nanocrystalline particles, the initiation of multiple shear bands is promoted. However the shear band propagation is not inhibited because the particles size is of the same order of magnitude with respect to the shear band width [6,11].

In the last five years, an innovative approach for producing new types of BMG composites was developed exploiting the presence of a phase separation in the liquid state. This can be typically achieved by introducing one pair of elements with a positive enthalpy of mixing between them and a negative enthalpy of mixing with all the others. In this way amorphous/amorphous [12,13] and amorphous/crystalline [14,15] composites can be obtained. Amorphous/crystalline composites can be produced when one of the two immiscible liquids, with a reduced glass forming ability (GFA), tends to crystallise during cooling while the other liquid, having a higher GFA, is able to amorphise. Furthermore, different length scales in the microstructure can be produced depending on the transformation mechanism which occurs: interconnected fractal microstructures are the result of a continuous transformation such as the spinodal decomposition, whereas droplet-type microstructures result from a nucleation and growth mechanism [16].

In this paper we investigated the silver-rich corner of the Ag-Cu-Zr ternary system with the aim of obtaining amorphous/crystalline composites, exploiting the stable miscibility gap in the liquid phase [17]. In fact, the Ag-rich liquid is expected to crystallise as ductile f.c.c.-Ag solid solution, whereas an amorphous matrix should form from the Ag-poor liquid, since complete glass formation was observed in the Cu-Zr-Ag system for Ag contents below 40 at.% [18,19]. The phase selection and the microstructures of four different alloys obtained at different cooling rates were interpreted on the basis of the recently reassessed ternary Ag-Cu-Zr phase diagram [17].

EXPERIMENTAL

Master alloy ingots with nominal composition (at.%) $Ag_{75}Cu_{11}Zr_{14}$ (alloy A), $Ag_{73}Cu_{17}Zr_{10}$ (alloy B), $Ag_{47.5}Cu_{22.5}Zr_{30}$ (alloy C), $Ag_{47.5}Cu_{30}Zr_{22.5}$ (alloy D) were prepared by arc melting the pure elements under Ar atmosphere. Each ingot was re-melted several times in order to obtain a good homogeneity. Rapid solidified ribbons (about 40 μm thick) were obtained by melt spinning using a wheel speed of 20 m/s in He atmosphere. Alloys A and B have a Ag content corresponding to 80% wt. which is the minimum legal content for applications in jewellery.

A PANalytical X'Pert X-ray diffractometer (XRD) with Cu K_α radiation was used for structural characterisation. The microstructure of master alloys and as spun ribbons was observed with a Leica Stereoscan 410 scanning electron microscope (SEM) equipped with a energy dispersion spectroscopy (EDS) microprobe (Oxford Instruments). In some cases the metallographic samples were chemically etched with a solution containing 30% NH_4OH, 25% H_2O_2 and 45% CH_3CH_2OH after mirror polishing to 1 μm. The thermal stability of the as spun ribbons was characterised by differential scanning calorimetry at 20 K/min using a Diamond DSC Perkin Elmer. Hardness of the alloys was evaluated by instrumented indentation using a load controlled Fischerscope HM2000 with a Vickers diamond pyramid. For the master alloys and the as spun ribbons, indents with depth of 2 μm were performed with a loading rate of 2 mN/s. In the case of the as spun ribbons, hardness profiles of the transversal section were obtained performing indents with depth of 0.2 μm along parallel rows at different distances from the ribbon surface. At least 8 measurements were performed for each series. For all the samples hardness values were extracted according to the standard ISO 14557-1. The capability of the ribbon to be plastically deformed was qualitatively estimated by bending test.

The thermodynamic calculations based on the CALPHAD technique [20] were performed using the FactSage software [21].

RESULTS

Fig. 1(i) and Fig. 1(ii) show the isopleths at 80 wt.% and 47.5 at.%, respectively. The predicted reaction sequence upon cooling of alloys A and C is the following

$L \rightarrow L_1 + L_2$ (separation in two liquids) (1)

$L_1 + L_2 \rightarrow L_1' + L_2' + AgZr$ (primary precipitation) (2)

L_1' (Ag-rich) $\rightarrow L_2'$ (Ag-poor) + AgZr + f.c.c.-Ag (monotectic reaction at ~900°C) (3)

L_2' (Ag-poor) + f.c.c.-Ag $\rightarrow$ AgZr + $AgCu_4Zr$ (peritectic reaction at ~ 850°C) (4)

$AgCu_4Zr$ + AgZr $\rightarrow$ $Cu_{10}Zr_7$ + Ag (peritectoid reaction just above 600°C) (5)

In the case of alloys B and D, the sequence is similar to the previous one, except for reactions 2 and 3 that are respectively substituted by

$L_1 + L_2 \rightarrow L_1' + L_2' + AgCu_4Zr$ (primary precipitation) (2')

L_1' (Ag-rich) $\rightarrow L_2'$ (Ag-poor) + $AgCu_4Zr$ + f.c.c.-Ag (monotectic reaction at ~900°C) (3')

The equilibrium phases predicted at room temperature for alloys A, C and D are f.c.c.-Ag, AgZr, $Cu_{10}Zr_7$, whereas those calculated for alloy B are f.c.c.-Ag, $AgCu_4Zr$, $Cu_{10}Zr_7$.

Fig. 2(i) shows the XRD patterns of the various master alloys. All the patterns show the presence of the crystallographic reflections of the f.c.c.-Ag solid solution (dotted vertical lines). The remaining peaks were assigned to the following phases: AgZr and $Cu_{10}Zr_7$ in alloy A; $Cu_{10}Zr_7$, $AgCu_4Zr$ (m-phase) in alloy B; AgZr in alloy C and in alloy D. For alloys C and D some XRD reflections could not be indexed.

The SEM micrographs of Fig. 3, obtained with the backscattered electrons signal, show the microstructures of the master alloys. In the case of alloy A, Fig. 3(a), the elongated needle of AgZr are the primary phase immersed in a matrix containing Ag and $Cu_{10}Zr_7$ formed during the monotectic reaction (3) and the peritectoid reaction (5), respectively. Fig. 3(b), corresponding to alloy B, shows a droplet-type microstructure resulting from the phase separation in the liquid state; the bright phase corresponds to the f.c.c.-Ag solid solution, whereas in the dark droplets two different mixtures of intermetallic compounds were found: AgZr, $Cu_{10}Zr_7$ and $AgCu_4Zr$ m-phase on the one hand (see top inset of Fig. 3(b)) and $AgCu_4Zr$, AgZr, $Cu_{10}Zr_7$ and $CuZr_2$ on the other hand (see bottom inset of Fig. 3(b)). The average composition of the dark droplets (about $Cu_{50}Zr_{30}Ag_{20}$ at.%), determined by EDS analysis, is similar in the whole sample independently of the microstructure. The microstructure of alloy C, Fig. 3(c), shows bright dendrites of silver, resulting from the undercooling of the liquid, in a matrix containing lamellae of AgZr and the ternary $AgCu_4Zr$ m-phase. After chemical etching, a fine

microstructure containing Ag, AgZr and $AgCu_4Zr$ is revealed at high magnification, as shown in the inset of Fig. 3(c). In alloy D, Fig. 3(d), the bright f.c.c.-Ag solid solution shows either a droplet like microstructure (see left inset of Fig. 3(d)) and a dendritic microstructure (see right inset of Fig, 3(d)). In the first case, the f.c.c.-Ag rich droplets are immersed in a coarse microstructure of AgZr, $Cu_{10}Zr_7$ and $AgCu_4Zr$ (left inset of Fig. 3(d)), while in the second case, the f.c.c.-Ag rich dendrites are surrounded by a finer microstructure, where only the coarse grains of $CuZr_2$ could be clearly recognised (right inset of Fig. 3(d)). The average composition of the dark matrix (about $Cu_{50}Zr_{30}Ag_{20}$ at.%), determined by EDS analysis, is similar in the whole sample independently of the microstructure. In all the four master alloys, the bright f.c.c. Ag-rich phase contains about 4 ± 1 at.% Cu and 1 ± 0.5 at.% Zr.

The effect of the rapid solidification by melt-spinning on the phase selection is shown by the XRD patterns of the as spun ribbons (Fig. 2(ii)). In the case of alloy A and alloy B, the crystallographic reflections are the same as for the master alloy. Both for alloy C and alloy D, the XRD patterns show the presence of a halo, typical of the amorphous phase, together with the peaks of the f.c.c.-Ag solid solution (dotted vertical lines).

The values of lattice parameter of the f.c.c. Ag-rich solid solution in the different master alloys and in the corresponding melt spun ribbons are reported in Table 1.

After rapid solidification, the microstructures of the as spun ribbons, shown by the backscattered electrons images in Fig. 4, are significantly finer with respect to those corresponding to master alloys. In the case of alloy A, Fig. 4(a), a phase contrast between the bright f.c.c.-Ag solid solution and the grey mixture of the intermetallic phases (AgZr and $Cu_{10}Zr_7$) is visible. In alloy B, Fig. 4(b), the microstructure shows, similarly to the master alloy, dark droplets (where the single phases could not be clearly resolved) immersed in a bright matrix of the f.c.c.-Ag solid solution. The dark droplets become progressively larger moving away from the wheel side of the ribbon. The elongated shape of the dark phase in the middle of the ribbon is probably an effect of the rapid rotation of the wheel. For alloy C, Fig. 4(c), the micrograph obtained after chemical etching shows fine precipitates of f.c.c.-Ag (less than 200 nm in diameter) dispersed in the featureless amorphous matrix in the middle of the ribbon. As shown by the inset, the size of the precipitates progressively decreases moving towards the edge of the ribbon, where the microstructure appears more homogeneous. Despite the presence of the microstructural gradient, the ribbon is chemically homogeneous along the transversal section as resulted from the EDS analysis. In the case of alloy D, fig. 4(d) shows a droplet-type microstructure deriving from the phase separation in the liquid already observed in the corresponding master alloy. The bright droplets (Ag-rich), dispersed in the grey amorphous matrix, become progressively larger from the wheel

side towards the centre of the ribbon. Because of the intimate interconnection between amorphous matrix and f.c.c.-Ag precipitates in alloy C, Fig. 4(c), it was not possible to evaluate precisely the composition of the amorphous matrix. In the case of alloy D, where the Ag-rich solid solution is less finely dispersed in the amorphous matrix with respect to the ribbon of alloy C, the composition of the amorphous phase was estimated to be around $Cu_{50}Zr_{25}Ag_{25}$.

The DSC traces of the as spun ribbons are shown in Fig. 5. In the case of alloy A, curve (a), the absence of exothermic signals in the DSC trace confirms that the sample is fully crystalline after quenching, as already suggested by the XRD results. The DSC trace of alloy B, curve (b), shows a weak exothermic peak (T_{onset} = 446°C, T_{peak} = 463°C, ΔH_x = 5 J/g), likely related to the crystallisation of a small amount of amorphous phase that could not be detected by XRD. In alloy C, the crystallisation of the amorphous phase detected by XRD occurs in two stages (T_{onset} = 422°C, T_{peak1} = 438°C, T_{peak2} = 497°C) and releases a total crystallisation enthalpy of about 47 J/g. Finally, in the case of alloy D, the crystallisation of the amorphous phase begins at T_{onset} = 478°C and shows two distinct peaks (T_{peak1} = 485°C and T_{peak2} = 574°C) together with a shoulder preceding the main signal. The total crystallisation heat is around 30 J/g.

The hardness values of the master alloys and the as spun ribbons, obtained from indents with a constant depth of 2 μm, are compared in table 1. In the case of the master alloy B and master alloy D, showing a coarse droplet-type microstructure, the Ag-poor phase (dark areas) are significantly harder than the Ag-rich phase (bright areas) because of the presence of the intermetallic phases previously identified by XRD and SEM. In the case of master alloy A and master alloy C, characterised by a more homogeneous microstructure, the hardness values can be considered representative of the whole system.

The hardness profiles along the transversal section of the ribbons, obtained performing indents with a constant depth of 0.2 μm, are shown in Fig. 6. The slight increase in hardness with respect to the values obtained with a depth of 2 μm is likely due to the so called indentation size effect [22]. In the case of alloys A, B and D the hardness is fairly constant along the ribbon section, whereas for alloy C the hardness increases near the two opposite edges of the ribbon.

All the alloys, except for alloy B, show a brittle behaviour upon bending.

DISCUSSION

The phase selection and the observed microstructure obtained under different cooling rates (slowly cooled master alloy and rapidly quenched ribbons) can be discussed on the basis of the calculated isopleths in Fig. 1 and Fig. 7.

In the case of alloy A, the phases detected both in the master alloy and in the ribbon are the equilibrium ones, as shown in Fig. 1(i) .

The presence of two different mixtures of phases in the dark droplets of master alloy B (AgZr + $Cu_{10}Zr_7$ + $AgCu_4Zr$ and $AgCu_4Zr$ + AgZr + $Cu_{10}Zr_7$ + $CuZr_2$) suggests that the Ag-poor liquid, whose composition (about $Cu_{50}Zr_{30}Ag_{20}$ at.%) was estimated from the EDS analysis of the dark droplets, followed different solidification paths. In the case of the dark droplets containing AgZr, $Cu_{10}Zr_7$ and $AgCu_4Zr$, we can assume that the Ag-poor liquid followed the solidification path of liquid-1, shown in Fig. 7, and was undercooled below ~ 800°C, bypassing the formation of primary $AgCu_4Zr$ and CuZr, but above ~ 625°C, avoiding the disappearance of AgZr. The formation of the dark droplets containing $AgCu_4Zr$ + AgZr + $Cu_{10}Zr_7$ + $CuZr_2$ can be explained by assuming that the Ag-poor liquid followed the solidification path of liquid-2 shown in Fig. 7. In this case, as a consequence of the primary precipitation of $AgCu_4Zr$, the remaining liquid becames progressively richer in Zr and could produce the observed phase mixture, containing $CuZr_2$, after being undercooled below ~ 700°C.

In the case of master alloy C, the presence of the ternary $AgCu_4Zr$ m-phase instead of $Cu_{10}Zr_7$ indicates that reaction 5 did not occur, probably because of the slow atomic mobility in the solid state.

Similarly to alloy B, also for alloy D the presence of two different phase mixture in the dark Ag-poor matrix can be explained by the two solidification paths (1 and 2) shown in Fig. 7.

Despite the phase separation in the liquid is expected to occur in all the four alloys, only alloys B and D show, both in the master alloys and the ribbons, microstructures that are representative of immiscibility. Interestingly, the two alloys (B and D) showing the phase separation lie on the same tie-line at the centre of the miscibility gap, whereas the other two alloys (A and C), that do not show evidence of a phase separation, lie on another tie-line that is closer to the border of the spinodal decomposition calculated at a temperature (725 K [17]) close to the experimental T_g [18,19]. Further investigations, such as DSC at high temperature, are needed to understand if the miscibility gap in the liquid was bypassed upon cooling or if the calculated existence range has been overestimated.

The rapid solidification led to a refinement of the microstructure in alloys A and B (80 wt.% Ag) and to the partial amorphisation in alloys C and D (47.5 at.% Ag). As expected, the glass formation is strongly reduced when the silver content increases since the complete glass formation occurs only for Ag contents lower than

40 at.% [18,19]. The small amount of amorphous phase detected by DSC in alloy B can be explained by the supposed high degree of undercooling that brought to the precipitation of $CuZr_2$ in the master alloy. In the case of alloys C and D, the lower Ag content allowed the second liquid to reach the composition range where glass formation is possible and to form the observed composite microstructure.

The cooling rate and the degree of undercooling also affect the values of the lattice constant, *a*, of the f.c.c. Ag-rich solid solution. In the case of the master alloys, the values of *a* (4.085 Å–4.087 Å) are close to those reported for pure silver (4.0853–4.0863 Å) [23-25]. The slight differences between the four alloys are likely due to small composition variations of composition in the f.c.c. Ag-rich solid solution that could not be easily detected by EDS. Furthermore, since the single addition of Cu and Zr has an opposite effect on the lattice constant of f.c.c.-Ag (decreasing [24,25] and increasing [26] the value of *a*, respectively), the addition of both elements leads to a reciprocal compensation, that depends on the relative quantities of Cu and Zr.

The difference among the values of the lattice constant in the rapidly solidified alloys can be explained by the different amounts of solute atoms that could be frozen in the f.c.c. solid solution, as a consequence of the rapid quenching. In particular, the significant decrease of *a* (4.082 Å) in the rapidly quenched alloy D can be interpreted by an increase of the Cu content in the f.c.c. solid solution with respect to the equilibrium conditions. .

Concerning the mechanical properties, the bending ductility of the ribbon of alloy B can be explained by the presence of a continuous ductile matrix of the f.c.c.-Ag solid solution. Furthermore, the rounded interface between the matrix and the intermetallic compounds likely reduces the stress concentration and inhibits the crack propagation. For the ribbons of the remaining alloys the brittle behaviour is probably due, in the case of alloy A, to the presence of the brittle AgZr intermetallic compounds and, in the case of alloys C and D, to the dominating brittle behaviour of the amorphous matrix.

The presence of a non negligible amount of hard intermetallic compounds in all master alloys brings to hardness values that are significantly higher than those of pure silver (60 HV) and commercial Sterling silver, 92.5 wt.% Ag, (140 HV). The hardness increase of the rapidly quenched alloys C and D with respect to the corresponding master alloys is due to the presence of the Ag-poor amorphous matrix. In fact, Cu–Zr–Ag BMGs (with a maximum 10 at.% Ag content) have Vickers hardness values between 534 and 599 [18]. The slightly different values measured for alloys C and D are due to the presence of different amounts of the soft f.c.c.-Ag solid solution. Finally, the slight hardness increase observed along the cross section of the ribbon of alloy C can be explained by the presence of a higher fraction of amorphous phase in the external zone of the

ribbon, as suggested by the micrograph of Fig. 4(c), where the quenching rate was higher because of the contact with the copper wheel on one side and the He atmosphere on the other.

CONCLUSIONS

Rapid solidification of silver-rich Ag–Cu–Zr alloys was exploited with the aim of entering a metastable liquid miscibilty gap and forcing the stabilisation of two undercooled liquids with very different compositions. Microstructural observations showed a clear phase separation only for the two alloys (B and D) that are located in the centre of the calculated miscibility gap. The formation of different phase mixtures in the Ag-poor regions of master alloys B and D is probably the consequence of different solidification paths, depending on the degree of undercooling. No evidence of liquid phase separation was detected for the two alloys (A and C) that lie on the tie-line approaching the border of the miscibility gap.

In the case of the rapidly solidified alloys C and D, with 47.5 at.% Ag, composites with f.c.c.-Ag rich precipitates in a Ag-poor amorphous matrix were obtained since the Ag-poor liquid could be successfully undercooled towards the glass forming composition range. For the rapidly solidified alloys A and B, richer in Ag (80 wt.%), a very small amount of amorphous phase was detected only in alloy B because of the tendency of the liquid to be deeply undercooled.

The significant increase in hardness, with respect to the corresponding slowly cooled master alloys, observed for the rapidly solidified alloys C and D is due to presence of the hard Ag-poor amorphous matrix.

Acknowledgements

The authors acknowledge financial support by MIUR (PRIN 2008).

References

[1] A. Inoue, Acta Mater. 48 (2000) 279

[2] F. Spaepen, Acta Metall. 25 (1977) 407

[3] F. Szuecs, C.P. Kim, W.L. Johnson, Acta Mater. 49 (2001) 1507

[4] C.C. Hays, C.P. Kim, W.L. Johnson, Mater. Sci. Eng. A 304-306 (2001) 650

[5] K.B. Kim, J. Das, F. Baier, M.B. Tang, W.H. Wang, J. Eckert, Appl. Phys. Lett 88 (2006) 051911

[6] A. Inoue, W. Zhang, T. Tsurui, A. R. Yavari, A. L. Greer, Phil. Mag. Lett. 85 (2005) 221

[7] D. V. Louzguine-Luzgin, A. Vinogradov, A. R. Yavari, S. Li, G. Xie, A. Inoue, Phil. Mag. 88 (2008) 2979

[8] E. Pekarskaya, C.P. Kim, W.L. Johnson, J. Mater. Res. 9 (2001) 2513

[9] C.A. Schuh, T.C. Hufnagel, U. Ramamurty, Acta Mater. 55 (2007) 4067

[10] G.Y. Sun, G. Chen, C.T. Liu, G.L. Chen, Scripta Mater. 55 (2006) 375

[11] A. Castellero, S.J. Lloyd, S.V. Madge, Zs. Kovacs, J.F. Löffler, M. Baricco, A.L. Greer, J. Alloys Compd. 434–435 (2007) 48

[12] A.A. Kundig, M. Ohnuma, D.H. Ping. T. Ohkubo, K. Hono, Acta Mater. 52 (2004) 2441

[13] N. Mattern, T. Gemming, J. Thomas, G. Goerigk, H. Franz, J. Eckert, J. Alloys Compd. 495 (2010) 299

[14] T. Kozieł, Z. Kędzierski, A. Zielińska-Lipiec, K. Ziewiec, Scripta Materialia 54 (2006) 1991

[15] J. He, H. Li, B. Yang, J. Zhao, H. Zhang, Z. Hu, J. Alloys Compd 489 (2010) 535

[16] R.D. Doherty in “Physical Metallurgy (vol. 2)”, R.W. Cahn and P. Haasen eds., North Holland, Amsterdam, 1996, pp. 1480-1490

[17] D.H. Kang, I.-H. Jung, Intermetallics 18 (2010) 815

[18] W. Zhang, A. Inoue, J. Mater. Res. 21 (2006) 234

[19] A.A. Kündig, M. Ohnuma, T. Ohkubo, T. Abe, K. Hono, Scripta Mater. 55 (2006) 449

[20] N. Saunders, A.D. Miodownik in “CALPHAD: a comprehensive guide”, N. Saunders ed., Pergamon, New York, 1998

[21] C.W. Bale, E. Belisle, P. Chartrand, S.A. Decterov, G. Eriksson, K. Hack et al., Calphad 33 (2009) 295

[22] D. Tabor, “The Hardness of Metals”, Clarendon Press, Oxford, 1951

[23] “Pearson’s Handbook of Crystallographic Data for Intermetallic Phases (vol. 2)”, P. Villars and L.D. Calvert eds., American Society for Metals, Matals Park (OH), 1985, p. 806

[24] “A Handbook of Lattice Spacings and Structures of Metals and Alloys”, W.B. Pearson ed., Pergamon Press, Oxford, 1964, pp. 278-279

[25] “A Handbook of Lattice Spacings and Structures of Metals and Alloys (vol. 2)”, W.B. Pearson ed., Pergamon Press, Oxford, 1967, p. 514

[26] Y.Y. Cui, T.L. Wang, K.P. Tai, B.X. Liu, J. Alloys Compd. 488 (2009) 223

TABLE CAPTIONS

Table 1. Lattice constant, *a*, of the f.c.c. Ag-rich solid solution.

Table 2. Vickers hardness values for the master alloys and the as spun ribbons. Indents with constant depth (2 μm) were performed at a loading rate of 2 mN/s.

FIGURE CAPTIONS

Fig. 1. Isopleths at 80 wt.% Ag (i) and 47.5 at.% Ag (ii) in the Ag-Cu-Zr system.

Fig. 2. XRD patterns (Cu K_α) of the master alloys (i) and the as spun ribbon (ii) for alloy A, curve (a), alloy B, curve (b), alloy C, curve (c), and alloy D, curve (d). The vertical dotted lines indicated the position of the crystallographic reflections of the f.c.c.-Ag solid solution.

Fig. 3. SEM micrographs (backscattered electrons signal) of the master alloys. (a): alloy A. (b): alloy B. (c): alloy C. (d): alloy D.

Fig. 4. SEM micrographs (backscattered electrons signal) of the as spun ribbons. (a): alloy A. (b): alloy B. (c): alloy C. (d): alloy D.

Fig. 5. DSC traces of the as spun ribbon at a heating rate of 20 K/min. (a): alloy A. (b): alloy B. (c): alloy C. (d): alloy D.

Fig. 6. Vickers hardness profiles obtained by instrumented indentation. Indents with constant depth (0.2 μm) were performed at a loading rate of 0.2 mN/s. (a): alloy A. (b): alloy B. (c): alloy C. (d): alloy D.

Fig. 7. Isopleth at 20 at% Ag in the Ag-Cu-Zr system.

Table 1

	f.c.c. Ag-rich solid solution lattice constant, *a* (Å)	
	Master alloy	As spun ribbon
Alloy A	4.087	4.088
Alloy B	4.085	4.084
Alloy C	4.087	4.085
Alloy D	4.086	4.082

Table 2

	Hardness (HVN)	
	Master alloy	Ribbon
Alloy A	195±14	243±11
Alloy B	144±40 (Ag-rich) 435±91 (Ag-poor)	249±14
Alloy C	370±23	533±21 (am.+ nano-Ag)
Alloy D	122±10 (Ag-rich) 440±42 (Ag-poor)	442±14 (am. + Ag)

Figure 1

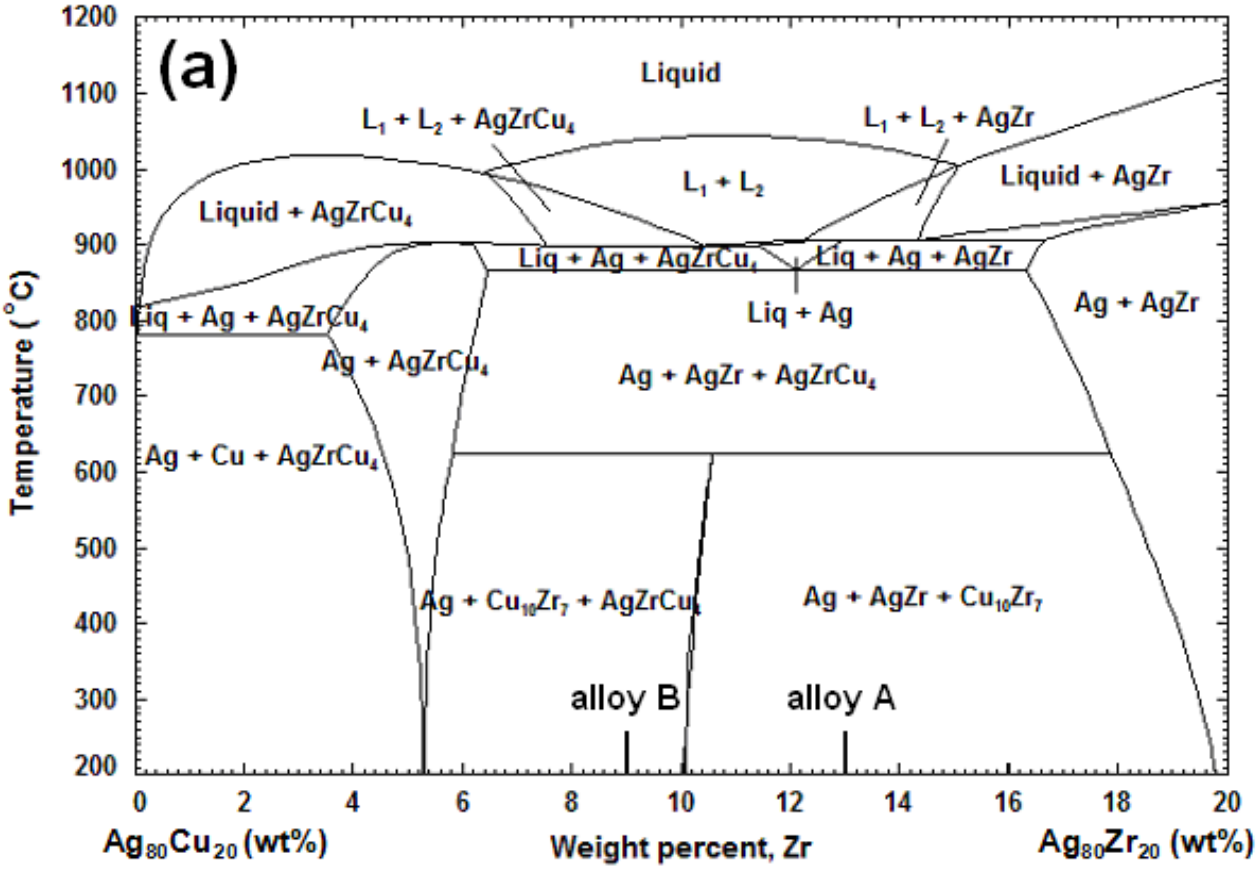
(a)
Liquid
L1 + L2 + AgZrCu4
L1 + L2 + AgZr
L1 + L2
Liquid + AgZr
Liquid + AgZrCu4
Liq + Ag + AgZrCu4
Liq + Ag + AgZr
Liq + Ag
Ag + AgZr
Liq + Ag + AgZrCu4
Ag + AgZrCu4
Ag + AgZr + AgZrCu4
Ag + Cu + AgZrCu4
Ag + Cu10Zr7 + AgZrCu4
Ag + AgZr + Cu10Zr7
alloy B
alloy A
Temperature (°C)
Ag80Cu20 (wt%)
Weight percent, Zr
Ag80Zr20 (wt%)

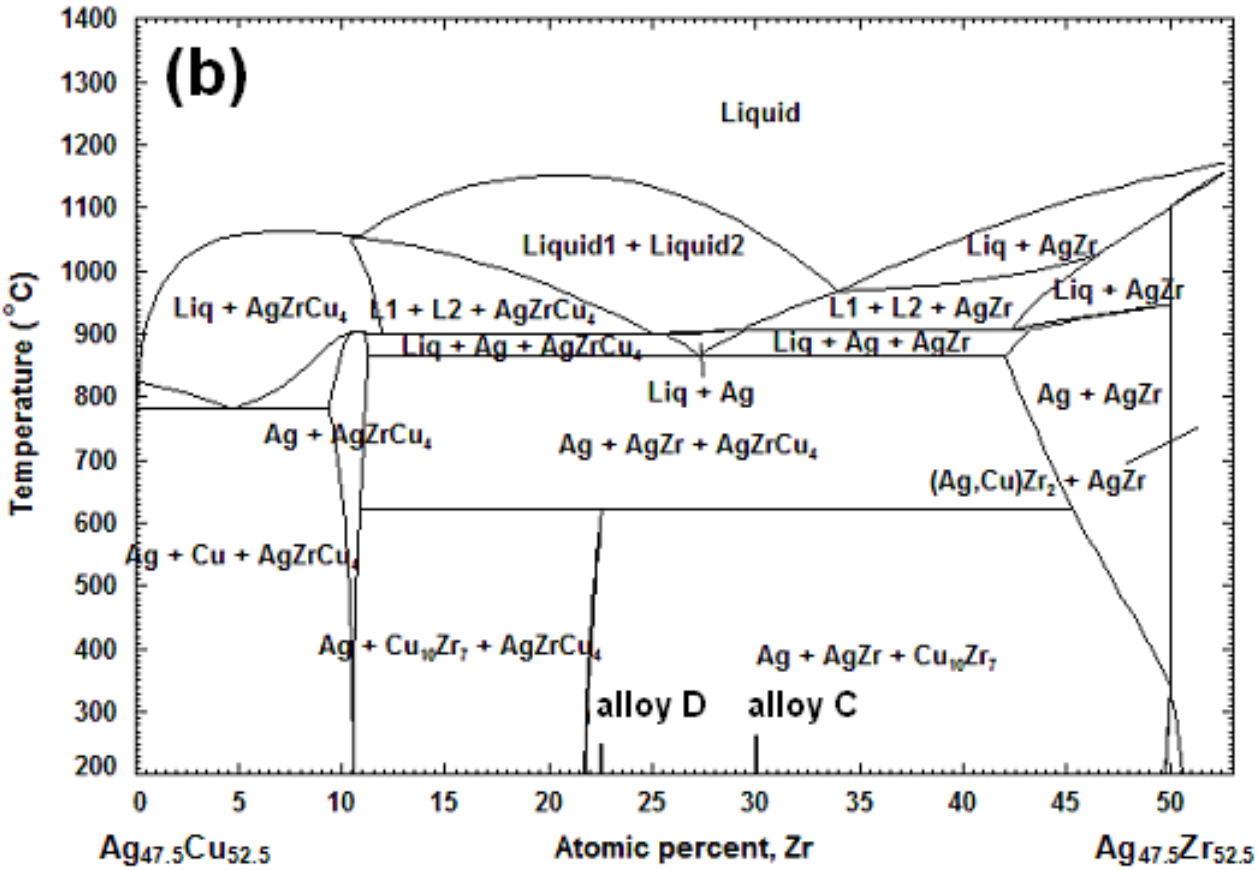
(b)
Liquid
Liquid1 + Liquid2
Liq + AgZr
Liq + AgZr
Liq + AgZrCu4
L1 + L2 + AgZrCu4
L1 + L2 + AgZr
Liq + Ag + AgZrCu4
Liq + Ag + AgZr
Liq + Ag
Ag + AgZr
Ag + AgZrCu4
Ag + AgZr + AgZrCu4
(Ag,Cu)Zr2 + AgZr
Ag + Cu + AgZrCu4
Ag + Cu10Zr7 + AgZrCu4
Ag + AgZr + Cu10Zr7
alloy D
alloy C
Temperature (°C)
Ag47.5Cu52.5
Atomic percent, Zr
Ag47.5Zr52.5

Figure 2

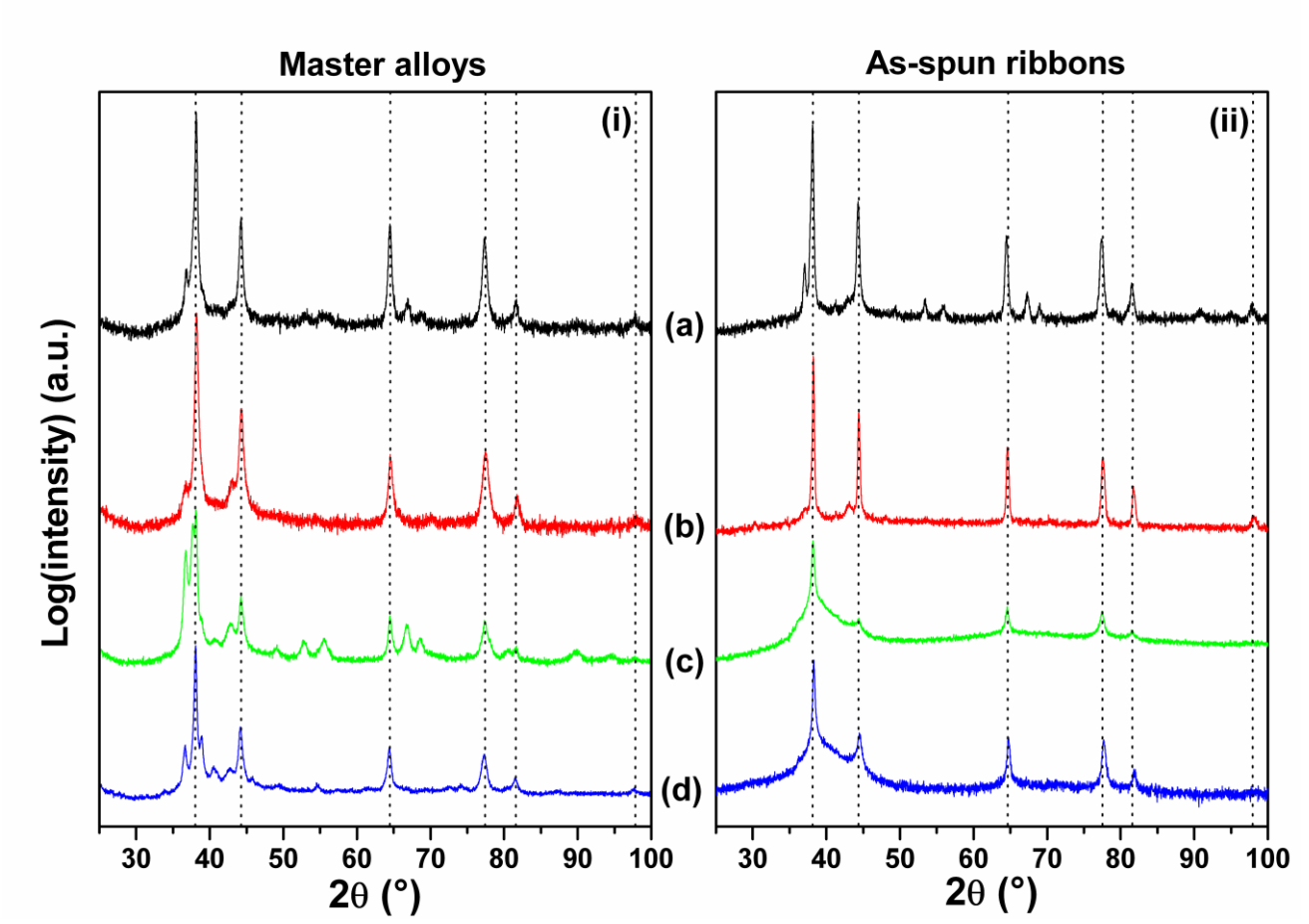
Master alloys
As-spun ribbons
(i)
(ii)
(a)
(b)
(c)
(d)
Log(intensity) (a.u.)
30
40
50
60
70
80
90
100
2θ (°)

Figure 3

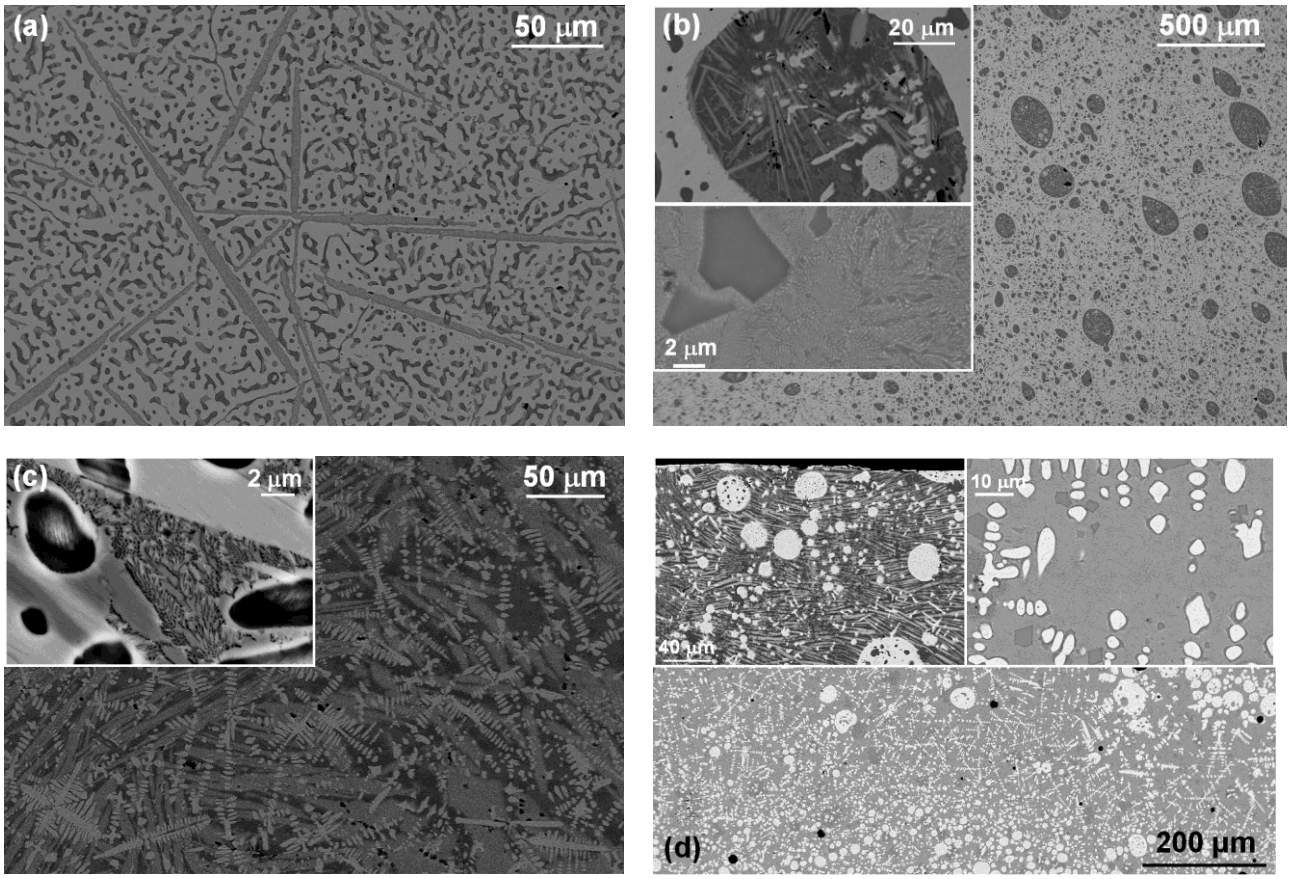

Figure 4

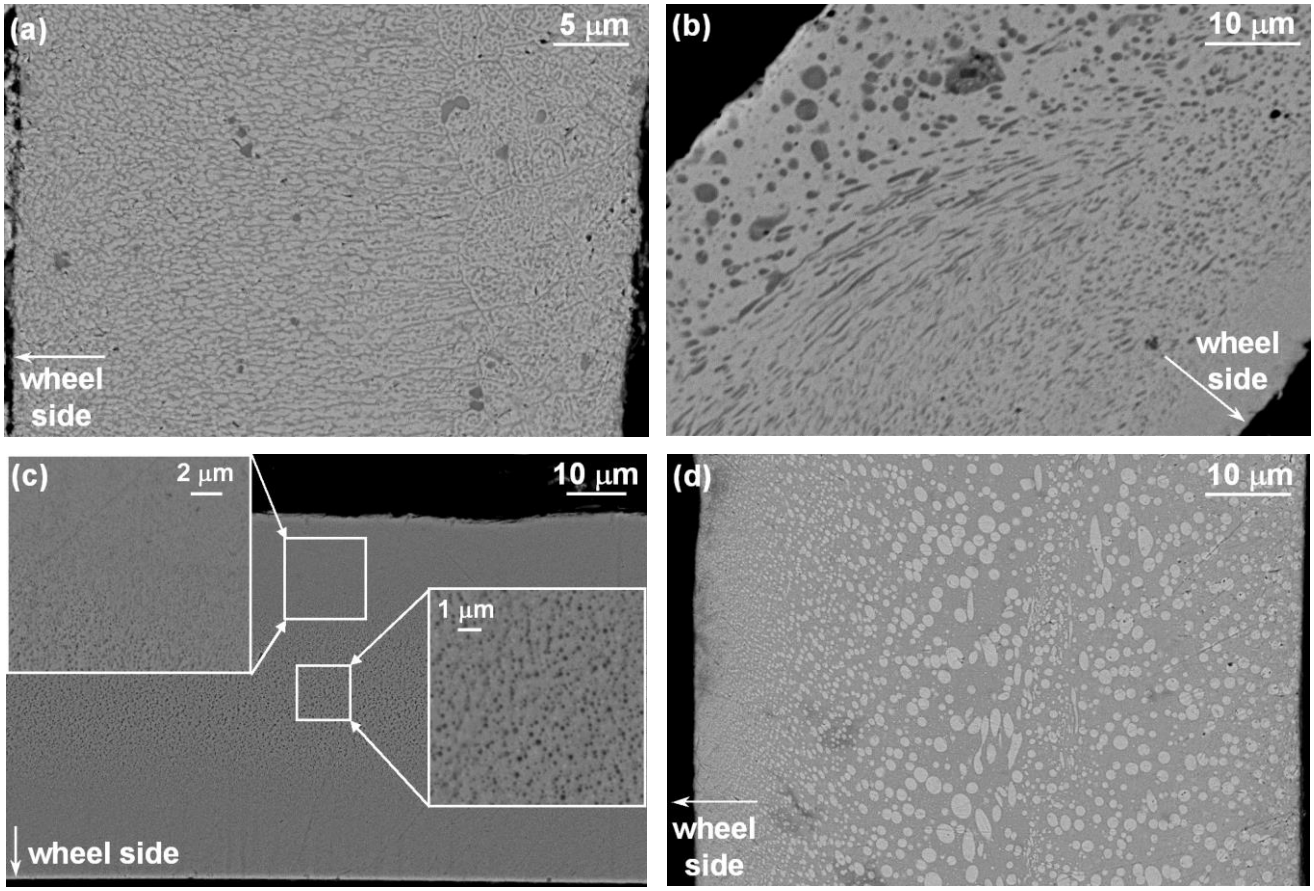
(a)
5 μm
wheel side
(b)
10 μm
wheel side
(c)
2 μm
10 μm
1 μm
wheel side
(d)
10 μm
wheel side

Figure 5

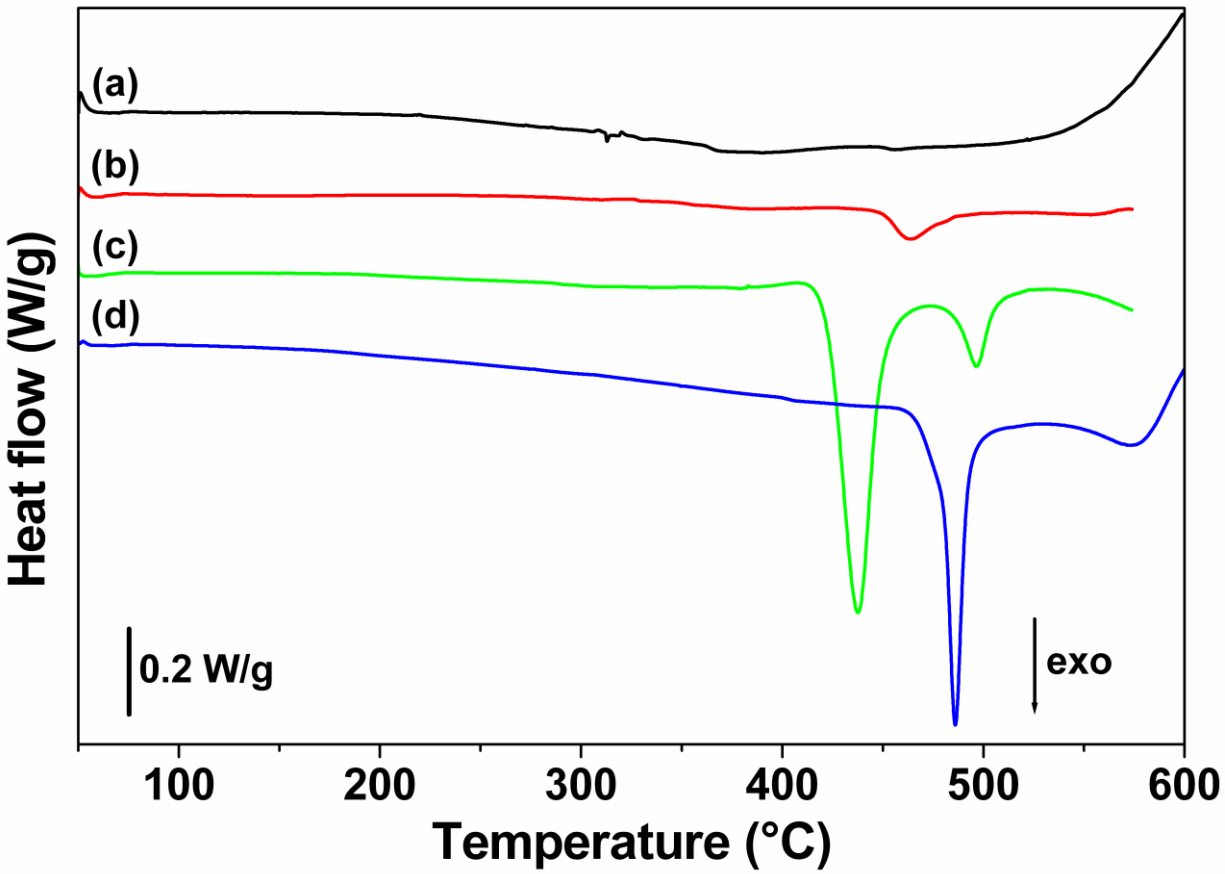
(a)
(b)
(c)
(d)
Heat flow (W/g)
0.2 W/g
exo
100
200
300
400
500
600
Temperature (°C)

Figure 6

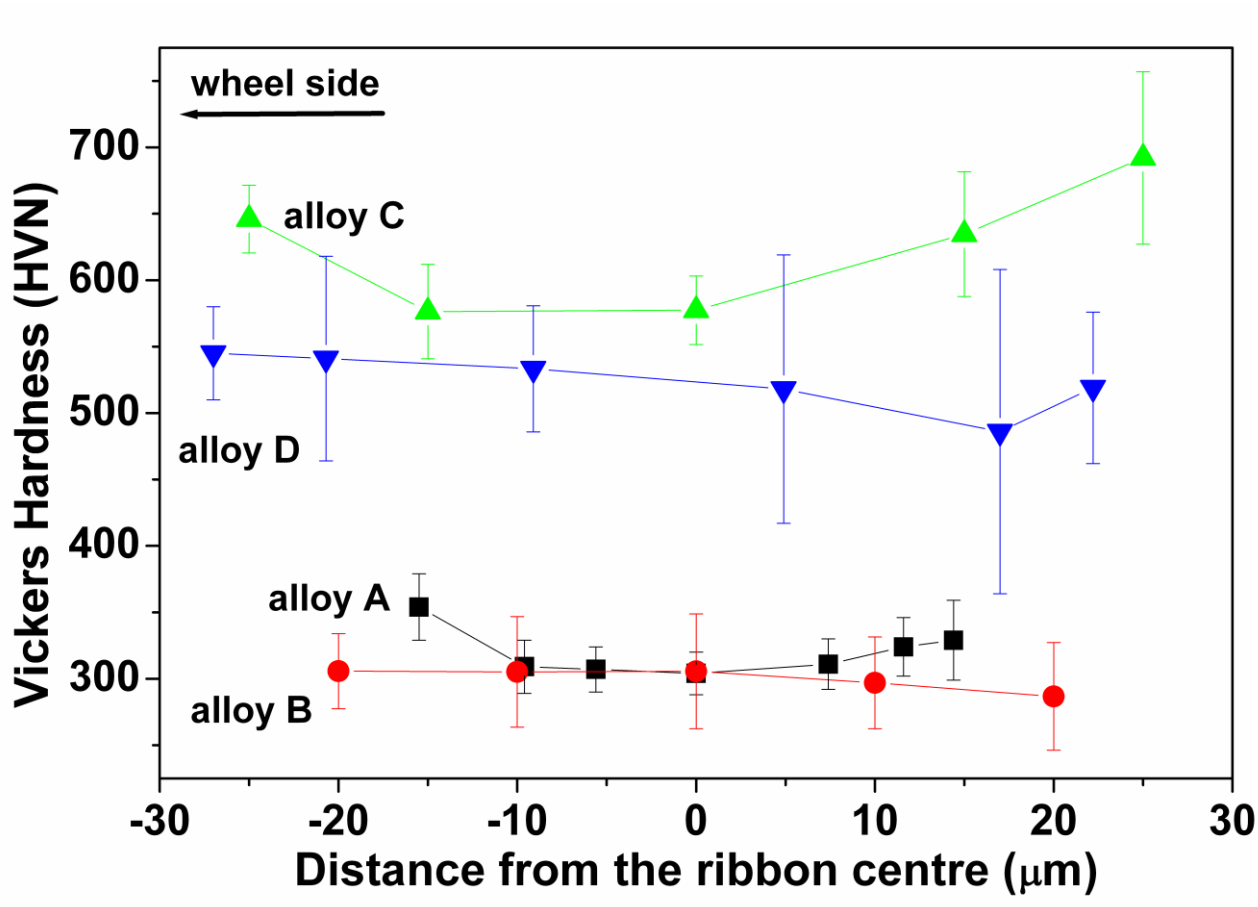
wheel side
alloy C
alloy D
alloy A
alloy B
Vickers Hardness (HVN)
700
600
500
400
300
-30
-20
-10
0
10
20
30
Distance from the ribbon centre (μm)

Figure 7

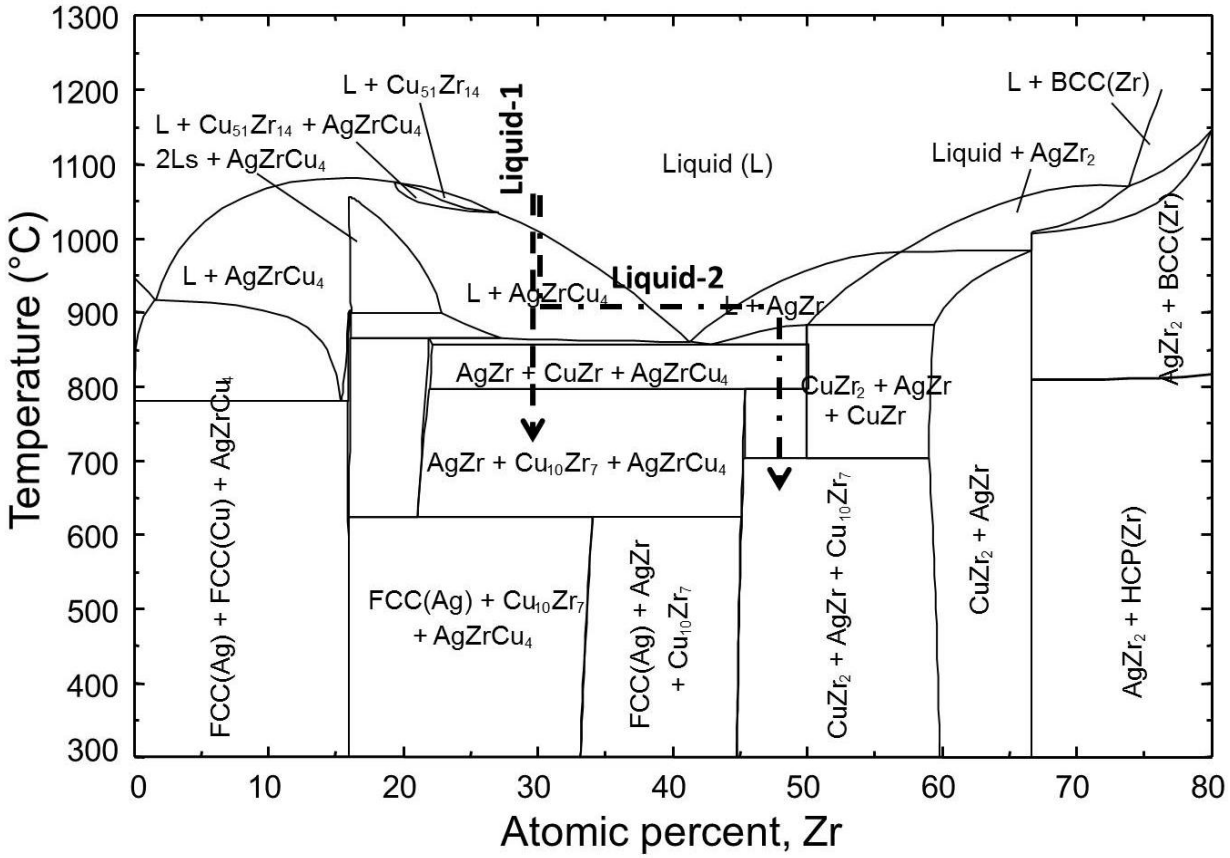
Temperature (°C)
Atomic percent, Zr
L + Cu51Zr14
L + Cu51Zr14 + AgZrCu4
2Ls + AgZrCu4
Liquid-1
Liquid (L)
L + BCC(Zr)
Liquid + AgZr2
L + AgZrCu4
L + AgZrCu4
Liquid-2
L + AgZr
AgZr2 + BCC(Zr)
AgZr + CuZr + AgZrCu4
CuZr2 + AgZr
+ CuZr
AgZr + Cu10Zr7 + AgZrCu4
FCC(Ag) + FCC(Cu) + AgZrCu4
FCC(Ag) + Cu10Zr7
+ AgZrCu4
FCC(Ag) + AgZr
+ Cu10Zr7
CuZr2 + AgZr + Cu10Zr7
CuZr2 + AgZr
AgZr2 + HCP(Zr)